ORIGINAL PAPER

Clean synthesis of biocarbon-supported Ni@Pd core–shell particles via hydrothermal method for direct ethanol fuel cell anode application

E. Leal da Silva[1,2] · A. Cuña[2] · C. Reyes Plascencia[2,3] · C. Radtke[4] · N. Tancredi[2,3] · C. de Fraga Malfatti[1]

Abstract

Direct ethanol fuel cells (DEFCs) are devices for clean and sustainable energy production, where the generation of electrical energy occurs as a result of the anodic ethanol oxidation reaction (EOR). One of the main challenges of these devices is the development of cost-effective and sustainable anodic catalysts, minimizing the use of noble metals such as Pd. In this sense, biomass-derived carbon-supported core–shell nanoparticles of PdNi-based electrocatalyst are of great interest for EOR and its application in DEFCs. The purpose of this work was to demonstrate the possibility of synthesizing a core–shell Ni@Pd electrocatalysts via hydrothermal method, in a fast, simple and environmental friendly way. A biomass hydrothermal lique-faction method using nickel and palladium salts was used to synthesize a biocarbon-supported nickel/palladium core–shell electrocatalyst (Ni@Pd/aHC). The electrocatalyst was morphological and chemical characterized in order to confirm the core–shell particle formation. The electrochemical characterization showed that the Ni@Pd/aHC sample has good elec-trocatalytic behaviour and good stability over time. The EOR mechanism on the sample and their influence in the faradaic efficiency of a cell were also studied by spectroelectrochemical analysis.

Graphic abstract
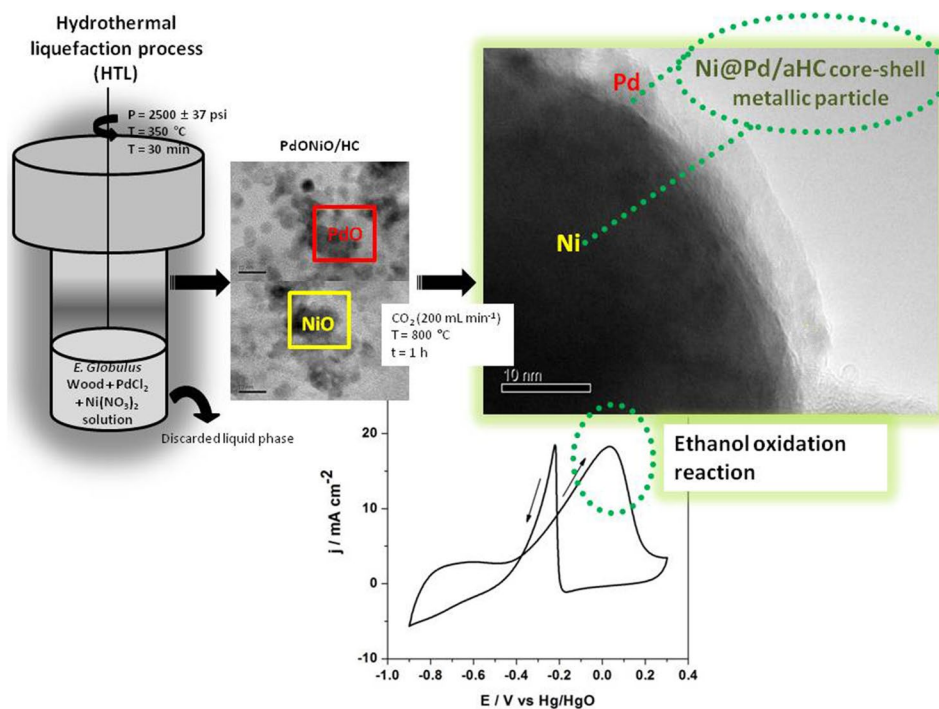
Extended author information available on the last page of the article

Introduction

Direct ethanol fuel cell (DEFC) is an environmentally friendly and energy efficient technology with application in electric devices, distributed power generation systems and electric vehicles, among others (Antolini and Gonzalez 2010). This type of fuel cell has some important advantages with respect to other fuel cells since it uses ethanol as fuel instead of hydrogen (Antolini 2007). Unlike hydrogen, ethanol is in a liquid state at room temperature and pressure, is cheaper and easier to obtain, and its transport and handling is easy. At the same time, the production of ethanol is quite widespread, especially in Brazil (Belincanta et al. 2016).

In DEFCs, the ethanol oxidation reaction (EOR) occurs in the anode of the cell with electrons release which produce an electrical current in an external electric circuit (Antolini and Gonzalez 2010). However, this reaction does not occur at an appreciable rate under standard conditions and therefore it requires the use of an adequate electrocatalyst. In alkaline medium, Pd (Hibbitts and Neurock 2013)-based electrocatalysts have been widely investigated for EOR, although the use of expensive metal such as Pd is not very suitable for commercial purposes. In this sense, one of a key goal for practical use of DEFCs is to find a non-noble metal-based and efficient EOR electrocatalyst. This could be achieved through the using of Pd alloys (Zalineeva et al. 2015), particularly PdM alloy where M is a non-noble metal which may act as a co-catalyst (Jongsomjit et al. 2016). In the last years, different works that study such materials have been reported, showing good perspectives for the case of electrocatalysts based on PdNi (Jongsomjit et al. 2016), PdSn (Zalineeva et al. 2015), PdCu (Hsieh and Whang 2013) and PdAg (Liu et al. 2012). Of these, due to its high electrochemical stability in alkaline media and low cost, nickel-based electrocatalysts are one of the most interesting and promising materials, although it is still necessary to optimize their electrocatalytic performance and to better understand the influence of the nickel on the PdNi compound (Chen et al. 2015).

On the other hand, in the last years, core–shell nanoparticles are of great significance in a wide range of applications including chemical catalysis (Chen et al. 2008). These types of materials are in nanometer size with different shapes and are formed by a core (inner material) and a shell (outer layer material). In general, the core and the shell materials are of different nature and properties (Chaudhuri and Santanu 2012), allowing to combine their chemical, electronic and mechanical properties which may improve some properties compared with the separate materials. From the point of view of the electrocatalysts applications, nanometer core–shell materials can be prepared with a non-noble metal core surrounded by a thin shell of a noble metal such as Ag (Xu et al., 2013), Pd (Zong et al. 2018) and Pt (Ali et al. 2017). This is very interesting since it allows a positive synergistic effect between the two metals, improving the physicochemical and catalytic properties of the electrocatalyst, while allowing the reduction of the amount of the noble metal. Nanoparticle core–shell materials can be prepared by different methods such as wet chemical reaction, reduction, solvothermal, modified Stöber and hydrothermal method, among others (Chaudhuri and Santanu 2012). In recent years, several authors have shown that core–shell nanoparticles for catalyst applications can be prepared via hydrothermal synthesis, e.g. TiO_2 (Jiang et al. 2016), gold–metal oxide (Lukosi et al. 2016), zeolites composite (Jin et al. 2018) or zeolite/silicalite (Liu et al. 2018). However, as far as we know, this method has not yet been evaluated for the PdNi core–shell-based EOR electrocatalyst preparation.

Thus, the main purpose of this work is to demonstrate the possibility of preparing a biocarbon-supported Ni@Pd core–shell particles (composed of a Ni core and Pd shell) via hydrothermal method for its application as an active material in DEFCs anode. In this way, for the first time in the literature, it is reported the preparation and physicochemical characterization of a core–shell PdNi-based electrocatalyst using this clean and simple method and its electrochemical and spectroelectrochemical evaluation as an EOR catalyst.

Experimental

Synthesis of Ni@Pd/HC electrocatalyst

The electrocatalyst sample was synthesized based on a previous work (Cuña et al. 2017) using stainless steel Parr 4575 reactor. The hydrothermal liquefaction (HTL) process was carried out at 623 K for 1800 s at self-generated pressure by water vapor and reaction gases. This method has an important advantage with respect to other methods for electrocatalysts synthesis (e.g. impregnation/reduction method) which generally needs to carry out more steps and involve pollutant chemical reagents (Modibedi et al. 2015). In this work, a 0.15 mol L^{-1} Ni(NO$_3$)$_2$ (99.98% Sigma-Aldrich) and a 0.04 mol L^{-1} PdCl$_2$ (99.99% Sigma-Aldrich) aqueous solution were mixed with *Eucalyptus globulus* wood biomass (from a 10-year-old tree from Bañado de Medina, Cerro Largo Department, Uruguay) using a solution/wood ratio of 22:1 (w/w). This raw material was selected due to

its abundance and availability in South America and other places. At the end of this first stage, an intermediate product was obtained which consists of a hydrochar-supported PdO-NiO (PdONiO/HC) compound. In order to activate the produced hydrochar and to reduce the metal oxides, this intermediate sample was submitted at CO_2 activation treatment at 1073 K for 3600 s, obtaining the activated hydrochar-supported Ni@Pd electrocatalyst (Ni@Pd/aHC). A blank sample was prepared without metal salts, following the same protocol described before, obtaining a hydrochar (HC) by HTL and an activated hydrochar (aHC) after CO_2 activation.

Physicochemical characterization

The morphological information of the samples was obtained with a JEOL 2100 TEM, (LaB6) 200 kV, equipped with a CCD GATAN ORIUS 1000 camera, and energy dispersive spectroscopy (EDS) probe with a 65 mm SDD detector. The Rutherford backscattering spectrometry (RBS) analyses were performed using a He^+ beam at 2 MeV produced by TANDEM accelerator of 3 MV. XPS analysis was performed with an Omicron surface analysis station equipped with a SPHERA hemispherical analyser and a DAR 400 Al K_α (1486.7 eV) X-ray source. The chamber was evacuated to 1×10^{-8} mbar during analysis. Pass energies were 50 and 10 eV for survey and high-resolution spectra, respectively. X-Ray diffraction (XRD) characterization was performed with a Rigaku Ultima IV equipment using a Cu $K_{\alpha 1}$ radiation ($\lambda = 1.54 \mathring{A}$). Thermogravimetric analysis (TGA) was made using Shimadzu TG-50 equipment in air atmosphere.

Electrochemical and Spectroelectrochemical characterization

The electrochemical characterization was performed at room temperature using a standard three-electrode cell, with Hg/HgO and platinum wire as reference and counter electrode, respectively. The mass of the analysed sample in the working electrode was 1.65×10^{-6} kg. The cyclic voltammetries were performed in a 1.0 mol L^{-1} NaOH solution and in a 1.0 mol L^{-1} ethanol + 1.0 mol L^{-1} NaOH solution with a scan rate of 50 mV s^{-1} in a potential range of -0.9 to $+0.3$ V versus Hg/HgO electrode. The electrocatalytic stability of the electrocatalyst was evaluated by a chronoamperometry analysis using the above mentioned basic ethanol solution. The electrochemical analyses were performed in an AUTO-LAB PGSTAT 302 N apparatus.

Taking into account that the EOR mechanism has a direct influence on the efficiency of the cell (Godoi et al. 2016), this mechanism for the prepared electrocatalyst was also studied by spectroelectrochemical analysis. In situ Fourier transform infrared spectroscopy in attenuated total reflectance mode (in situ ATR-FTIRS) measurements was carried

using a Bruker Vertex 70 V equipment. The experimental set-up used in this work was similar to that used by Leal da Silva et al. (2016). The three-electrode cell and ethanol-based electrolyte are the same as those used in electrochemical characterizations.

Results and discussion

Physicochemical results

PdONiO/HC as obtained by HTL was analysed by TEM-EDS; Fig. 1 shows different zone areas of the sample. These results demonstrate that PdONiO/HC has a heterogeneous morphology and chemical composition. On the one hand, according to the chemical composition determined by EDS, there are areas with nanoparticles rich in Pd and O with an average size of 6.1 nm (see Fig. 1a) and, on the other hand, zone areas with nanoparticles rich in Ni and O with average
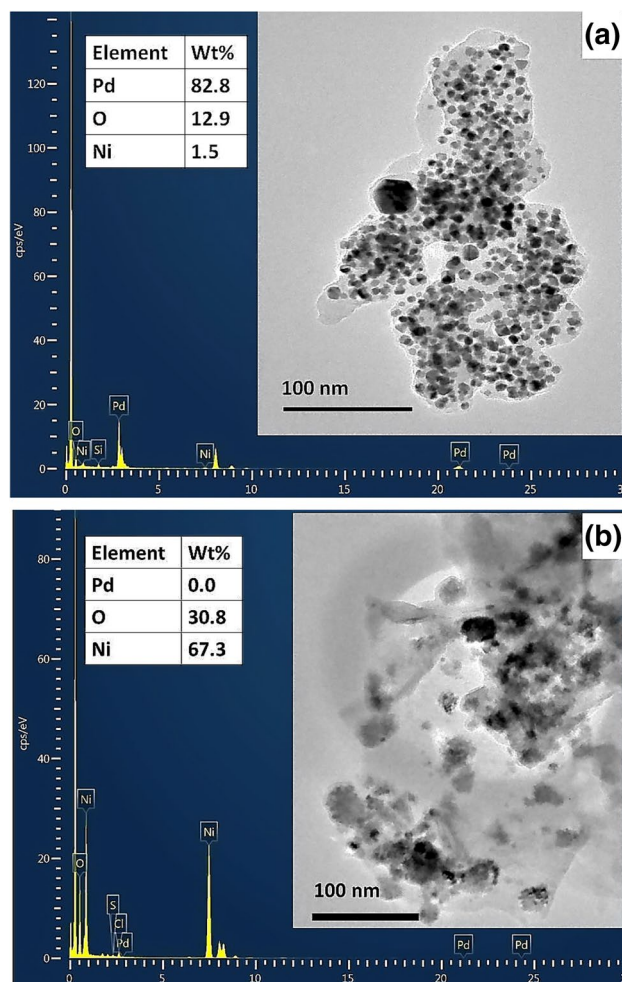

Fig. 1 EDS spectra and TEM micrograph images (inset) of different analysed zones of the PdONiO/HC sample

size of 8.3 nm (see Fig. 1b). Figure 2a, b shows HRTEM images of the nanoparticles seen in Fig. 1a. In these images, an interplanar distance of 0.26 nm can be determined, which is consistent with crystalline structure of PdO particles (Guo et al. 2011). On the other hand, the HRTEM images (Fig. 2c, d) of the nanoparticles shown in Fig. 1b present crystalline structures with an interplanar distance of 0.28 nm, which is consistent with the presence of NiO particles (Cuña et al. 2017). It can be concluded that PdONiO/HC sample was composed of PdO and NiO nanoparticles dispersed in different zones of the sample.
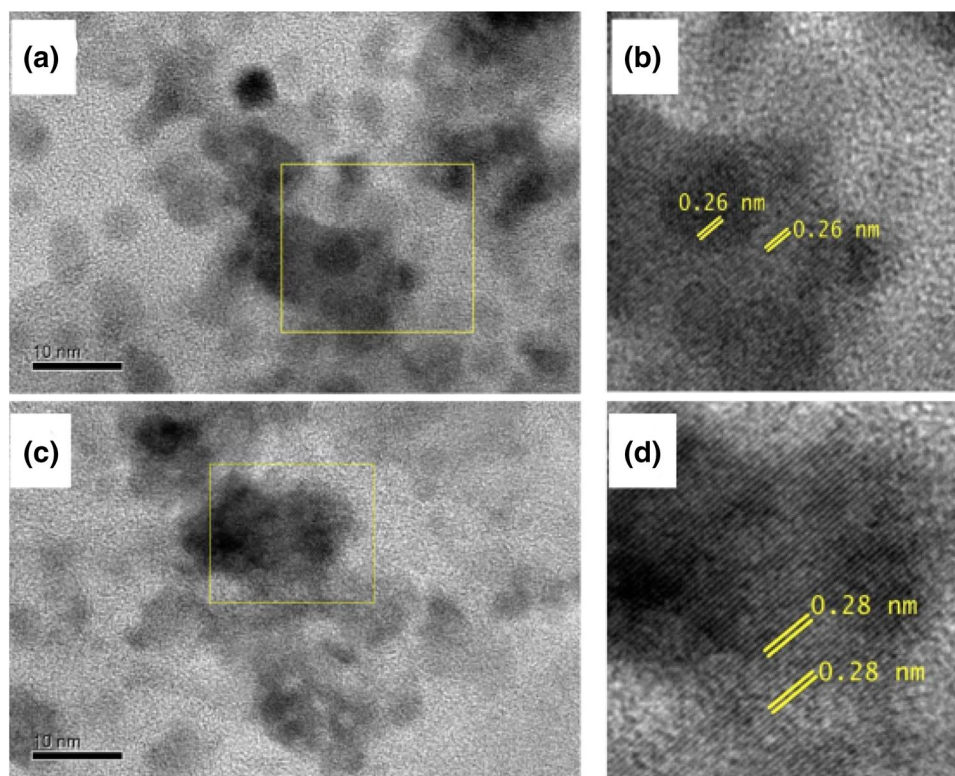
The TEM micrographs images of the Ni@Pd/aHC sample, obtained after CO_2 activation treatments, are shown in Fig. 3a. In this case, the homogeneous morphology and composition could be observed in the whole analysed sample. Large nanoparticles with average size of 266 nm were observed. EDS analysis indicated that they are composed mainly of Ni (78.2 wt%) and Pd (20.2 wt%). This result is consistent with the particles percentage mass composition determined by RBS: 85% Ni and 15% Pd. HRTEM analysis showed that these particles do not have a homogeneous structure (see Fig. 3b). The centre of the particles showed crystalline structures with an interplanar distance of 0.21 nm (see Fig. 3c) consistent with the crystalline structure of metallic Ni (Argueta-Figueroa et al. 2014), while the particles edge showed an interplanar distance of 0.25, consistent with the crystal structure of Pd (Sebastian et al. 2016). Thus, these physicochemical characterizations confirm that Ni@Pd

core–shell particles can be obtained following the synthesis proposed in this work.

Figure 4 shows Ni 2p regions of XPS spectra of PdO-NiO/HC and Ni@Pd/aHC samples. The shaded area of the figure corresponds to the binding energy region of the Ni $2p^{3/2}$ component. Comparing the signal of both samples in this region, one can clearly observe the effect of the CO_2 activation treatment at 800 °C for 1 h. The spectrum of the PdONiO/HC sample evidences Ni in a high oxidation state that probably corresponds to Ni in the form of oxides or hydroxides. For the Ni@Pd/aHC sample, the signal in the Ni $2p^{3/2}$ region is shifted to a lower binding energy, which indicates lower oxidation of the Ni present in this sample (Biesinger et al. 2011). However, there is no evidence of Ni^0 in the resulting spectra. Pd was not analysed since it was below the sensitivity of our equipment.

The X-ray diffractogram of Ni@Pd/aHC is shown in Fig. 5. Peaks at 44.4°, 51.8° and 76.4° correspond to the (111), (200) and (220) planes of Ni° crystal (Xu et al. 2007). Remaining NiO particles were confirmed from the peaks at 37.0° and 62.8° indexed as (111) and (220) crystal planes (Zhang et al. 2016). The peaks at 40.0°, 46.6°, 68.0°, 81.94° and 86.48° are indexed as (111), (200), (220), (311) and (222) crystal planes of the face-centred cubic (fcc) structure of Pd (Su et al. 2015). The low intensity of the Pd^0 peaks in the diffractogram indicates that it is present in low quantities, which in agreement with the fact that Pd has not been detected by XPS

Fig. 2 HRTEM micrograph images of different zone areas of the PdONiO/HC sample obtained by HTL. **a** and **b** correspond to the zone analysed in Fig. 1a. **c** and **d** correspond to the zone analysed in Fig. 1b
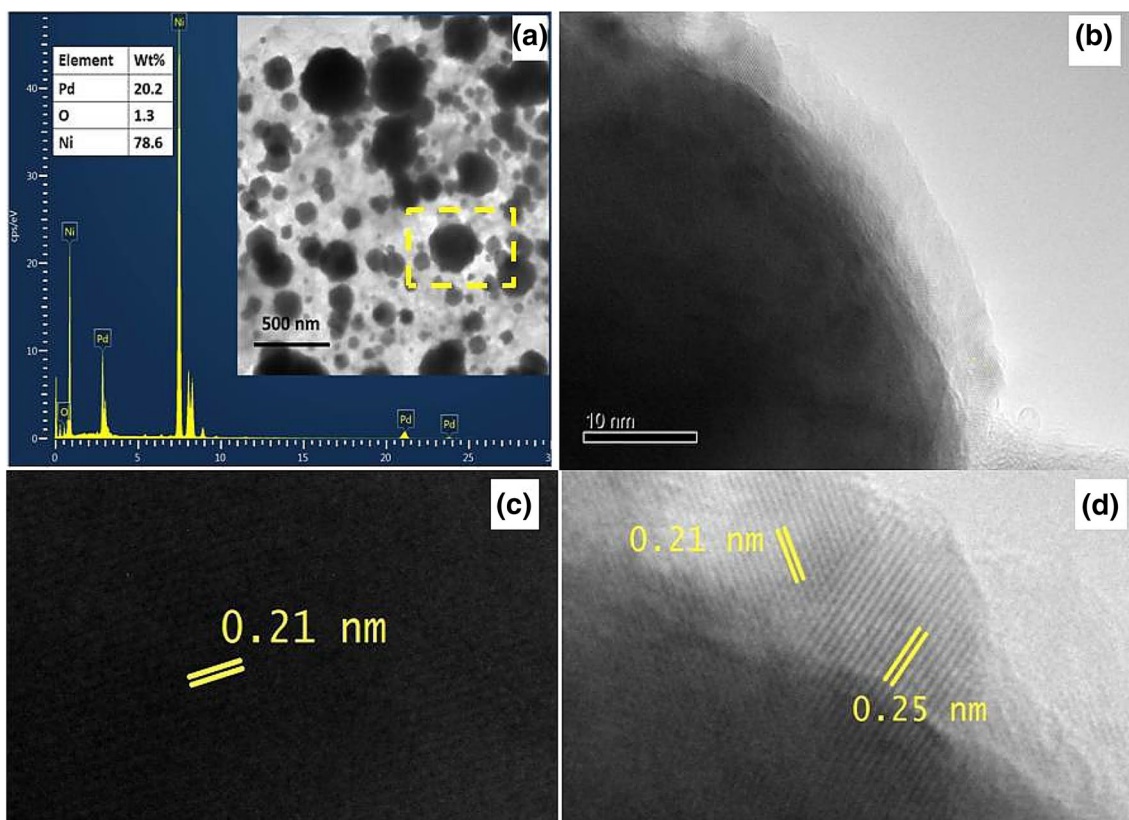
Fig. 3 **a** EDS spectrum and TEM micrograph image (inset) of the Ni@Pd/aHC sample obtained by HTL after thermal and CO_2 activation treatments; **b** HRTEM image of a selected particle [indicated with a rectangle in (**a**)]; **c** centre of the particle; **d** edge of the particle
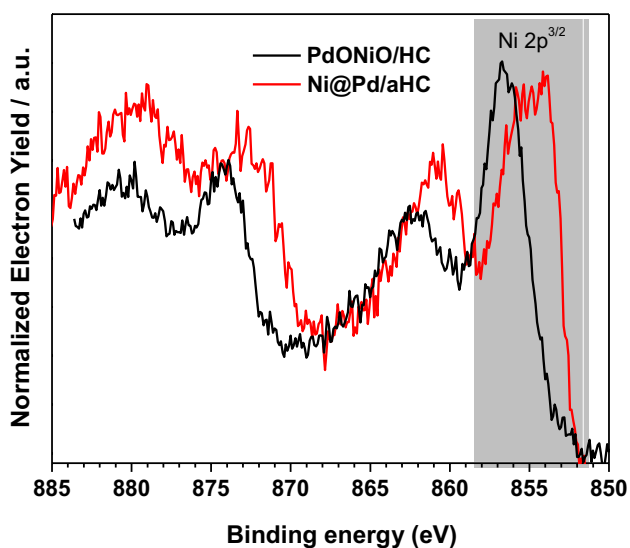

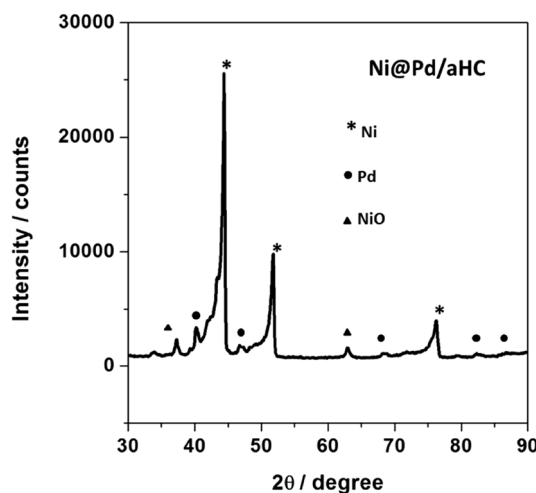**Fig. 4** Ni 2p regions of XPS spectra of PdONiO/HC and Ni@Pd/aHC samples

Fig. 5 XRD patterns of Ni@Pd/aHC electrocatalyst

analysis. XRD diffraction confirms the results obtained by HRTEM and EDS analysis, but is contradictory with the fact that Ni^0 was not detected in the XPS analysis.

A possible interpretation of this is that the Ni^0 is coated by a thin layer of nickel oxide, with enough thickness to avoid the Ni^0 detection through the XPS analysis (Cuña et al. 2017).

Figure 6 shows the thermogravimetric curves obtained in air atmosphere for PdONiO/HC, Ni@Pd/aHC, HC and aHC samples. For the last three samples, the ash content can be associated with the remaining mass in the, respectively, curve. Based on this, it is determined that the PdONiO content in the PdONiO/HC sample is 49.7%. Besides, the curve observed for the Ni@Pd/aHC electrocatalyst showed a different behaviours with respect to the other samples. In this sample, a mass increase can be observed from 873 K, which can be associated with the reaction of the metallic particles with oxygen during the TGA experiment. In this
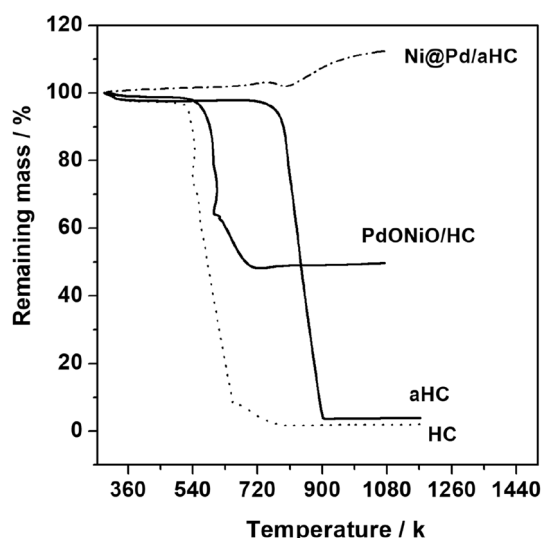
way, PdO and NiO particles are formed which determine the mass increase observed in the TGA curve. This result is in accordance with the XRD and TEM-EDS analysis and allows to confirm that the Ni@Pd/aHC electrocatalyst was mainly composed of Pd and Ni metal particles.

Electrochemical and spectroelectrochemical characterization

The voltammogram obtained for the Ni@Pd/aHC sample in 1.0 mol L^{-1} NaOH solution is shown in Fig. 7a. It has the typical shape of a Pd catalyst in alkaline medium (Hibbitts and Neurock 2013) rather than one corresponding to a Ni catalyst. Therefore, this obtained voltammogram does not exhibit the reversible formation of peaks of a reversible nickel oxyhydroxide formation (Cuña et al. 2017). Instead, three potential peaks could be observed during the anodic sweep, which corresponded to different electrochemical processes occurring on the surface of the Ni@Pd/aHC sample. Features during the forward sweep were observed to be present in similar potential regions for the Pd catalyst (Liang et al. 2009). In the voltammogram (Fig. 7a), an oxidation current is clearly observed in the potential range between -0.9 and -0.5 V versus Hg/HgO which is attributed to the oxidation of the absorbed and adsorbed hydrogen on the catalyst surface (Modibedi et al. 2011). The peak above -0.2 V can be attributed to the formation of PdO layer on the surface of the Pd^0 particles (Liang et al. 2009). The sharp cathodic peak at -0.3 V versus Hg/HgO can be attributed to the reduction of the PdO formed in the anodic sweep (Liang et al. 2009).

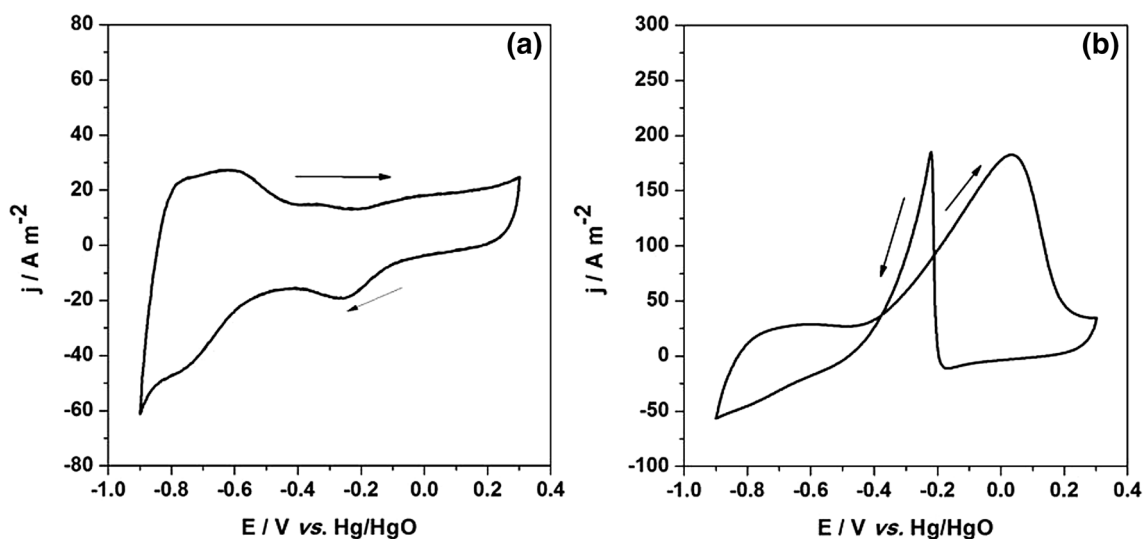

Fig. 6 Thermogravimetric curves of PdONiO/HC, Ni@Pd/aHC, HC and aHC

Fig. 7 Cyclic voltammetry curves of the Ni@Pd/aHC at a scan rate of 50 mV s^{-1} in **a** 1.0 mol L^{-1} NaOH; **b** 1.0 mol L^{-1} NaOH + 1.0 mol L^{-1} ethanol

The cyclic voltammetry of the Ni@Pd/aHC sample in a solution of 1.0 mol L^{-1} NaOH and 1.0 mol L^{-1} ethanol is shown in Fig. 7b. The voltammograms show the typical electrochemical behaviour for EOR on a palladium-based electrocatalyst (Shen et al. 2010) where Pd is the active catalyst, with two oxidation peaks: one in the anodic sweep related with the EOR, and the other in the cathodic sweep related with the oxidation of the EOR intermediates, generated during the anodic sweep (Kim et al. 2008) or with the remaining ethanol which has not been oxidized in anodic sweep (Iwasita 2002). This result is in accordance with the morphological and chemical analysis results where it was concluded that the prepared catalyst nanoparticles consist in a nickel core surrounded by an Pd shell (the active site of the EOR catalysis). If there were free Ni particles (without a Pd coverage), these particles could act as a catalytic site, and therefore, the shape of the voltammograms would be different, since, as is well known, the electrochemical behaviour of Ni as an EOR catalyst (Cuña et al. 2017) is clearly different from the behaviour of Pd-based catalysts (Leal da Silva et al. 2018). In the anodic sweep, the current begins to increase significantly from −0.35 V versus Hg/HgO up to a maximum value of 180 A m^{-2} at 0.03 V. This value of −0.35 V may be related to the onset potential (E_{onset}) of the EOR on the Ni@Pd/aHC surface and is very similar to the values reported for other Pd and PdNi-based electrocatalysts (Zhang et al. 2011).

The ATR-FTIR spectra obtained in ethanol/alkaline medium at different potentials are shown in Fig. 8, where different peaks can be observed depending on the applied potential. From bibliographic data, each peak can be associated with a certain functional group which can also be associated with the appearance of a certain product or intermediate products of the EOR. These results are summarized in Table 1.

According to this result, the acetate ion begins to appear from −0.3 V versus Hg/HgO that is consistent with the onset potential determined from the voltammogram present in Fig. 7b. At the potential of −0.1 V, it is possible to observe a slight increase in the peak intensity associated with the acetaldehyde. The acetaldehyde peak intensity is much less than that observed for the acetate ion peaks. This would show that during the EOR very small amount of acetaldehyde is formed as reaction product or it is an intermediate with a short lifetime. In the ATR-FTIR spectra, it is also possible to identify a negative peak at 1046 cm^{-1}, which is related to ethanol consumption (Plyler 1952). It is well known that CO_2 formation is usually associated with a peak at 2342 cm^{-1} in the FTIR spectra. In this case, no peak is detected at any applied potential; therefore in this case, the ethanol oxidation is not occurring until the CO_2 formation. Based on these results, and taking into account previous reported works (Godoi et al. 2016), the most likely
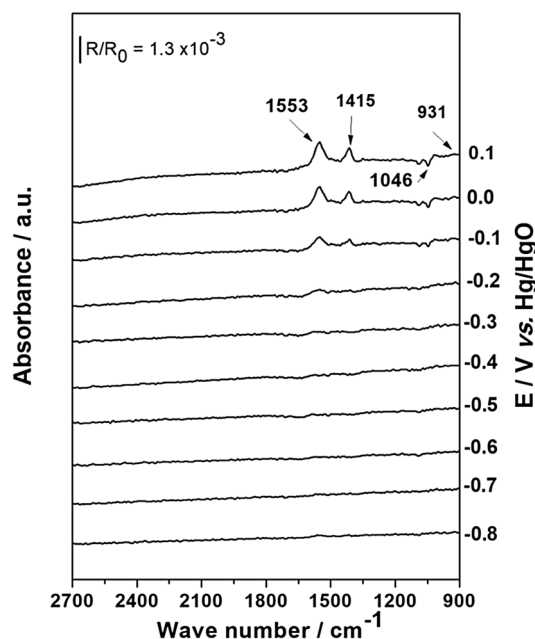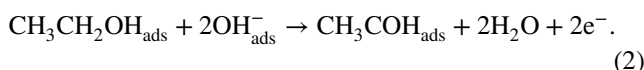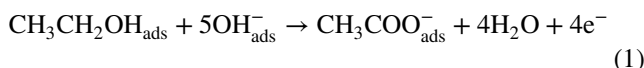

Fig. 8 In situ ATR-FTIR spectra taken in the potential range −0.8 to 0.1 V versus Hg/HgO in 1 mol L^{-1} NaOH + 1.0 mol L^{-1} ethanol. Backgrounds were collected at −0.8 V (vs. Hg/HgO)

EOR mechanism on the Ni@Pd/aHC electrocatalyst can be expressed as follows:

$$CH_3CH_2OH_{ads} + 5OH_{ads}^- \rightarrow CH_3COO_{ads}^- + 4H_2O + 4e^- \tag{1}$$

$$CH_3CH_2OH_{ads} + 2OH_{ads}^- \rightarrow CH_3COH_{ads} + 2H_2O + 2e^-. \tag{2}$$

This mechanism determines a lower faradaic efficiency (ε_F) for the cell, since instead of the EOR occurring towards the total oxidation to give CO_2 and releasing 12 electrons, the oxidation of ethanol occurs by releasing between two (when acetaldehyde is formed) and four electrons (when acetate ion is formed) (Altarawneh et al. 2018). ε_F can be determined according to the following equation (Altarawneh et al. 2017):

$$\varepsilon_F = \frac{\sum n_i f_i}{12} \tag{3}$$

where n_i is the number of electrons exchanged in the product i formation and f_i is the fraction of ethanol that is transformed into the product. Although in this work we have not carried out a quantitative analysis to quantify formed products in relation to the amount of oxidized ethanol, these relation can be estimated from the intensity of the corresponding peaks in the FTIR spectra. The peak intensities of the acetaldehyde and the acetate ion as a function of the potential are shown in Fig. 9. It can be clearly seen that from −0.3 to −0.1 V versus Hg/HgO, the peaks corresponding to acetate

Table 1 Main peaks observed during the ATR-FTIRS analysis and their associated species. The potential at which it begins to see the peak (E_{onset}) is indicated in the first column

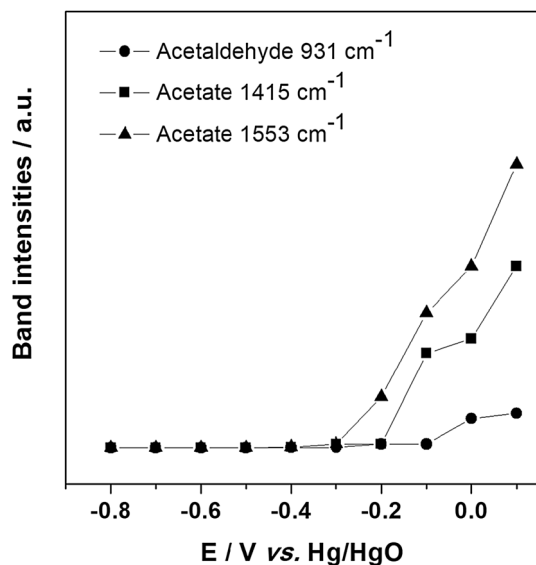| E_{onset}/V versus Hg/HgO	Peak λ/cm^{-1}	Associated chemical functional group vibration	Associated EOR group
−0.3 V	1415 cm^{-1}	C–O (symmetric)	Acetate ion (Godoi et al. 2016)
−0.3 V	1553 cm^{-1}	C–O (asymmetric)	Acetate ion (Godoi et al. 2016)
−0.1 V	931 cm^{-1}	O–C–O stretching	Acetaldehyde (Leung et al. 1989)

Fig. 9 Acetaldehyde and acetate band intensities as a function of the potential for the Ni@Pd/aHC sample

Fig. 10 Current–time curve for Ni@Pd/aHC in 1.0 mol L^{-1} NaOH + 1.0 mol L^{-1} ethanol at −0.1 V versus Hg/HgO

ion have values much higher than for the acetaldehyde whose peak does not have an appreciable intensity. Therefore, in this potential range, the acetate ion can be considered as the only product of the EOR (100% of the oxidized ethanol is transformed into acetate ion). Thus, for this case, and according to Eq. 3, ε_F is equal to 0.33. From −0.1 V, the intensity of the peak corresponding to acetaldehyde begins to increase although always below the intensity of the acetate peaks. Then, from this potential, we can consider that ethanol is oxidized to give acetaldehyde in addition to acetate. In this way, for the ε_F calculation, the proportion f_i in which the ethanol is oxidized to give each of the products must be taken into account. Thus, for an applied potential of 0.1 V versus Hg/HgO, if we consider the intensity of the peak at 1553 cm^{-1} for acetate and 931 cm^{-1} for acetaldehyde, the fraction of ethanol that is converted into acetate would be equal to 88.5%, while the fraction to acetaldehyde is 11.5%. Thus, the value of ε_F calculated according to Eq. 3 is 0.31. These efficiency values are lower than those determined by other authors for similar materials (Altarawneh et al. 2018) which can be explained by the fact that the catalyst studied in this work does not favor a total oxidation of ethanol to give CO_2 and 12 electrons. Finally, it is important to note
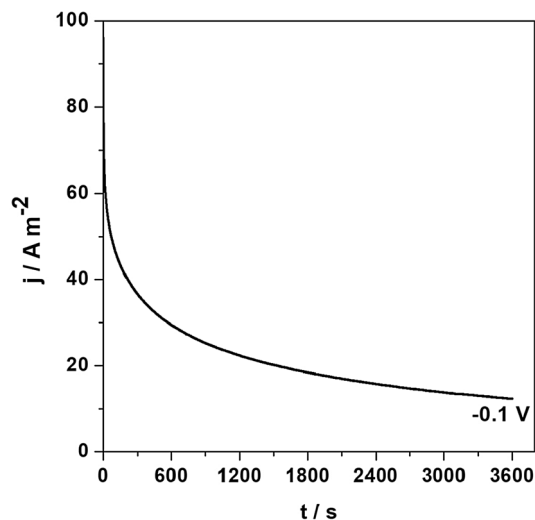
that here we have calculated ε_F by estimating the amounts of ethanol that is converted to each products. To make a more precise determination of ε_F, it must be necessary to make quantitative determinations of f_i considering a mass balance of the EOR. In addition to this, it must be kept in mind that for calculation of the overall efficiency of the cell (ε_{DEFC}), should also be considered the theoretical efficiency (ε_{rev}) and the potential efficiency (ε_E) as well as ε_F (Altarawneh et al. 2018).

The current–time curve for the EOR in the Ni@Pd/aHC electrocatalyst performed at a fixed potential of −0.1 V versus Hg/HgO during 3600 s, showing in Fig. 10, indicates that there is a slow decrease in the current density during ethanol electro-oxidation over time, which is associated with a good electrocatalytic stability of the electrocatalyst.

Conclusions

In this work, we demonstrate that it is possible to obtain a Ni@Pd core–shell particles-based electrocatalyst via hydrothermal method using biomass as carbon support precursor. This synthesis is easy, clean and involves fewer steps than the other commonly reported synthesis. The electrochemical characterization shows that the synthesized electrocatalyst

has a good electrocatalitic behaviour as EOR electrocatalyst in alkaline medium and also with a good stability. The E_{onset} of the EOR and the maximum oxidation current determined for the sample were comparable to those reported for other electrocatalysts. Acetate ion is the main product in the EOR on the prepared Ni@Pd/aHC electrocatalyst, which implies a lower faradic efficiency. Future works should aim to improve this last aspect of the electrocatalyst.

References

Ali S, Khan I, Khan SA, Sohail M, Ahmed R, Rehman A, Ansari MS, Morsy MA (2017) Electrocatalytic performance of Ni@Pt core–shell nanoparticles supported on carbon nanotubes for methanol oxidation reaction. J Electroanal Chem 795:17–25

Altarawneh RM, Majidi P, Pickup PG (2017) Determination of the efficiency of ethanol oxidation in a proton exchange membrane electrolysis cell. J Power Sources 351:106–114

Altarawneh RM, Brueckner TM, Chen B, Pickup PG (2018) Product distributions and efficiencies for ethanol oxidation at PtNi octahedral. J Power Sources 400:369–376

Antolini E (2007) Catalysts for direct ethanol fuel cells. J Power Sources 170:1–12

Antolini E, Gonzalez ER (2010) Alkaline direct alcohol fuel cells. J Power Sources 195:3431–3450

Argueta-Figueroa L, Morales-Luckie RA, Scougall-Vilchisc RJ, Olea-Mejí OF (2014) Synthesis, characterization and antibacterial activity of copper, nickel and bimetallic Cu–Ni nanoparticles for potential use in dental materials. Prog Nat Sci 24:321–328

Belincanta J, Alchorne JÁ, Teixeira da Silva M (2016) The Brazilian experience with ethanol fuel: aspects of production, use, quality and distribution logistics. Braz J Chem Eng 33:1091–1102

Biesinger MC, Payne BP, Grosvenor AP, Lau LWM, Gerson AR, Smart RSC (2011) Resolving surface chemical states in XPS analysis of first row transition metals, oxides and hydroxides: Cr, Mn, Fe, Co and Ni. Appl Surf Sci 257:2717–2730

Chaudhuri RG, Santanu P (2012) Core/shell nanoparticles: classes, properties, synthesis mechanisms, characterization, and applications. Chem Rev 112:2373–2433

Chen Y, Yang F, Dai Y, Wang W, Chen S (2008) Ni@Pt core–shell nanoparticles: synthesis, structural and electrochemical properties. J Phys Chem C 112:1645–1649

Chen W, Zhang Y, Wei X (2015) Catalytic performances of PdNi/MWCNT for electrooxidations of methanol and ethanol in alkaline media. Int J Hydrogen Energy 40:1154–1162

Cuña A, Reyes Plascencia C, Leal da Silva E, Marcuzzo J, Khan S, Tancredi N, Baldan MR, Malfatti CF (2017) Electrochemical and spectroelectrochemical analyses of hydrothermal carbon supported nickel electrocatalyst for ethanolelectro-oxidation in alkaline medium. Appl Catal B 202:95–103

Godoi DRM, Villullas HM, Zhu F-C, Jiang Y-X, Sun S-G, Guo J, Sun L, Chen RA (2016) Comparative investigation of metal-support interactions on the catalytic activity of Pt nanoparticles for ethanol oxidation in alkaline medium. J Power Sources 311:81–90

Guo X, Zhi G, Yan X, Jin G, Guo X, Brault P (2011) Methane combustion over Pd/ZrO2/SiC, Pd/CeO2/SiC, and Pd/Zr0.5Ce0.5O2/SiC catalysts. Catal Commun 12:870–874

Hibbitts DD, Neurock M (2013) Influence of oxygen and pH on the selective oxidation of ethanol on Pd catalysts. J Catal 299:261–271

Hsieh MW, Whang TJ (2013) Electrodeposition of PdCu alloy and its application in methanol electro-oxidation. Appl Surf Sci 270:252–259

Iwasita T (2002) Fuel cells: spectroscopic studies in the electrocatalysis of alcohol oxidation. J Braz Chem Soc 13:401–409

Jiang J, Zhou H, Zhang F, Fan T, Zhang D (2016) Hydrothermal synthesis of core–shell TiO2 to enhance the photocatalytic hydrogen evolution. Appl Surf Sci 368:309–315

Jin W, Ma J, Ma H, Li X, Wang Y (2018) Hydrothermal synthesis of core–shell ZSM-5/SAPO-34 composite zeolites and catalytic performance in methanol-to-aromatics reaction. J Solid State Chem 267:6–12

Jongsomjit S, Prapainainar P, Sombatmankhong K (2016) Synthesis and characterisation of Pd–Ni–Sn electrocatalyst for use in direct ethanol fuel cells. Solid State Ionics 288:147–153

Kim JH, Choi SM, Nam SH, Seo MH, Choi SH, Kim WB (2008) Influence of Sn content on PtSn/C catalysts for electrooxidation of C1eC3 alcohols: synthesis, characterization, and electrocatalytic activity. Appl Catal B Environ 82:89–102

Leal da Silva E, Cuña A, Ortega Vega MR, Radtke C, Machado G, Tancredi N, Malfatti CF (2016) Influence of the support on PtSn electrocatalysts behaviour: ethanol electro-oxidation performance and in situ ATR-FTIRS studies. Appl Catal B 193:170–179

Leal da Silva E, Cuña A, Khan S, Marcuzzo J, Pianaro S, Cadorin M, Malfatti CF (2018) Biomass derived carbon as electrocatalyst support for ethanol oxidation reaction in alkaline medium: electrochemical and spectroelectrochemical characterization. Waste Biomass Valoriz. https://doi.org/10.1007/s12649-018-0510-8

Leung L-W, Chang SC, Weaver MJ (1989) Real-time FTIR spectroscopy as an electrochemical mechanistic probe: electrooxidation of ethanol and related species on well-defined Pt (111) surfaces. J Electroanal Chem 266:317–336

Liang ZX, Zhao TS, Xu JB, Zhu LD (2009) Mechanism study of the ethanol oxidation reaction on palladium in alkaline media. Electrochim Acta 54:2203–2208

Liu J, Zhou H, Wang Q, Zeng F, Kuang Y (2012) Reduced graphene oxide supported palladium–silver bimetallic nanoparticles for ethanol electro-oxidation in alkaline media. J Mater Sci 47:2188–2194

Liu C, Long Y, Wang Z (2018) Optimization of conditions for preparation of ZSM-5@silicalite-1 core–shell catalysts via hydrothermal synthesis. Chin J Chem Eng 26:2070–2076

Lukosi M, Zhu H, Dai S (2016) Recent advances in gold-metal oxide core–shell nanoparticles: synthesis, characterization, and their application for heterogeneous catalysis. Front Chem Sci Eng 10(1):39–56

Modibedi RM, Masombuka T, Mathe MK (2011) Carbon supported Pd–Sn and Pd–Ru–Sn nanocatalysts for ethanol electro-oxidation in alkaline medium. Int J Hydrogen Energy 36:4664–4672

Modibedi RM, Mehlo T, Ozoemena KI, Mathe MK (2015) Preparation, characterisation and application of Pd/C nanocatalyst in passive alkaline direct ethanol fuel cells (ADEFC). Int J Hydrogen Energy 40:15605–15612

Plyler EK (1952) Infrared spectra of methanol, ethanol, and n-propanol. J Res Natl Bur Stand 48:281–286

Sebastian V, Smith CD, Jensen KF (2016) Shape-controlled continuous synthesis of metal nanostructures. Nanoscale 8:7534–7543

Shen SY, Zhao TS, Xu JB, Li YS (2010) Synthesis of PdNi catalysts for the oxidation of ethanol in alkaline direct ethanol fuel cells. J Power Sources 195:1001–1006

Su N, Chen X, Ren Y, Yue B, Wang H, Cai W, He H (2015) The facile synthesis of single crystalline palladium arrow-headed tripods and their application in formic acid electro-oxidation. Chem Commun 51:7195–7198

Xu C, Shen PK, Liu Y (2007) Ethanol electrooxidation on Pt/C and Pd/C catalysts promoted with oxide. J Power Sources 164:527–531

Xu C, Yuan Y, Cui A, Yuan R (2013) In situ controllable synthesis of Ag@AgCl core–shell nanoparticles on graphene oxide sheets. J Mater Sci 48:967–973

Zalineeva A, Serov A, Serov MX, Martinez U, Artyushkova K, Baranton S, Coutanceau C, Atanassov P (2015) Nano-structured Pd-Sn catalysts for alcohol electro-oxidation in alkaline medium. Electrochem Commun 57:48–51

Zhang Z, Xin L, Sun K, Li W (2011) Pd-Ni electrocatalysts for efficient ethanol oxidation reaction in alkaline electrolyte. Int J Hydrogen Energy 36:12686–12697

Zhang L, Mu J, Wang Z, Li G, Zhang Y, He Y (2016) One-pot synthesis of NiO/C composite nanoparticles as anode materials for lithium-ion batteries. J Alloys Compd 671:60–65

Zong Z, Xu K, Li D, Tang Z, He W, Liu Z, Wang X, Tian Y (2018) Peptide templated Au@Pd core-shell structures as efficient bifunctional electrocatalysts for both oxygen reduction and hydrogen evolution reactions. J Catal 361:168–176

Affiliations

E. Leal da Silva[1,2] [ID] · **A. Cuña[2]** · **C. Reyes Plascencia[2,3]** · **C. Radtke[4]** · **N. Tancredi[2,3]** · **C. de Fraga Malfatti[1]**

✉ E. Leal da Silva
  elenlealdasilva@gmail.com

A. Cuña
acuna@fq.edu.uy

C. Reyes Plascencia
carmina@fq.edu.uy

C. Radtke
claudio.radtke@ufrgs.br

N. Tancredi
nestor@fq.edu.uy

C. de Fraga Malfatti
celia.malfatti@ufrgs.br

[1]   LAPEC/PPGE3M, Universidade Federal do Rio Grande do Sul, Av. Bento Gonçalves, 9500 setor 4, prédio 75, sala 232, Porto Alegre, RS 91501-970, Brazil

[2]   Area Fisicoquímica, DETEMA, Facultad de Química, Universidad de la República, Avenida General Flores 2124, CC 1157, 11800 Montevideo, Uruguay

[3]   Instituto Polo Tecnológico de Pando, Facultad de Química, Universidad de la República, Camino Saravia s/n, 91000 Pando, Uruguay

[4]   Instituto de Química, Universidade Federal do Rio Grande do Sul, Av. Bento Gonçalves 9500, Porto Alegre, RS 91501-970, Brazil